Monthly Notices of the ROYAL ASTRONOMICAL SOCIETY

MNRAS **507,** 104–115 (2021) https://doi.org/10.1093/mnras/stab2126
Advance Access publication 2021 July 24

High tide: a systematic search for ellipsoidal variables in ASAS-SN

D. M. Rowan [1,2]★ K. Z. Stanek,[1,2] T. Jayasinghe [1,2] C. S. Kochanek,[1,2] Todd A. Thompson [1,2] B. J. Shappee,[3] T. W. -S. Holoien [4] and J. L. Prieto[5,6]

[1]*Department of Astronomy, The Ohio State University, 140 West 18th Avenue, Columbus, OH 43210, USA*
[2]*Center for Cosmology and Astroparticle Physics, The Ohio State University, 191 W. Woodruff Avenue, Columbus, OH 43210, USA*
[3]*Institute for Astronomy, University of Hawaii, 2680 Woodlawn Drive, Honolulu, HI 96822, USA*
[4]*Carnegie Observatories, 813 Santa Barbara Street, Pasadena, CA 91101, USA*
[5]*Núcleo de Astronomía de la Facultad de Ingeniería y Ciencias, Universidad Diego Portales, Av. Ejército 441, Santiago, Chile*
[6]*Millennium Institute of Astrophysics, Santiago, Chile*

Accepted 2021 July 12. Received 2021 July 2; in original form 2021 May 5

ABSTRACT

The majority of non-merging stellar mass black holes are discovered by observing high energy emission from accretion processes. Here, we pursue the large, but still mostly unstudied population of non-interacting black holes and neutron stars by searching for the tidally induced ellipsoidal variability of their stellar companions. We start from a sample of about 200 000 rotational variables, semiregular variables, and eclipsing binary stars from the All-Sky Automated Survey for Supernovae. We use a χ^2 ratio test followed by visual inspection to identify 369 candidates for ellipsoidal variability. We also discuss how to combine the amplitude of the variability with mass and radius estimates for observed stars to calculate a minimum companion mass, identifying the most promising candidates for high mass companions.

Key words: binaries: close – stars: variables: general.

1 INTRODUCTION

There are an estimated 10^8–10^9 stellar mass black holes (BHs) in the Milky Way (Timmes, Woosley & Weaver 1996; Wiktorowicz et al. 2019). Stellar mass BHs are thought to be produced largely by direct collapse without a supernova (e.g. Ugliano et al. 2012; Pejcha & Thompson 2015). Two candidates for such a failed supernova were identified by Gerke, Kochanek & Stanek (2015) and Neustadt et al. (2021; also see Adams et al. 2017; Basinger et al. 2020), as a part of the search for 'vanishing' stars proposed by Kochanek et al. (2008). Double neutron star (NS) mergers, such as G170817 (Abbott et al. 2017), are also a channel of stellar mass BH formation (Pooley et al. 2018). Searches for stellar mass BHs are crucial for characterizing the end states of evolved massive stars, the underlying compact object mass distribution, and the intermediate evolutionary states before compact object mergers.

Stellar mass BHs are typically observed in X-ray binary systems (e.g. Remillard & McClintock 2006) or in gravitational wave detections of compact object mergers (e.g. Abbott et al. 2016). The `BlackCat` catalogue currently includes 69 X-ray emitting BH binaries (Corral-Santana et al. 2016). Most of those systems with mass estimates have masses of 5–10 $M_\odot$ with a low mass gap from $\sim$2 to 5 $M_\odot$ that separates the NS and stellar mass BH populations (Bailyn et al. 1998; Özel et al. 2010; Farr et al. 2011; Kochanek 2014). Between the first Gravitational Wave Source Catalogue (GWTC-1; Abbott et al. 2019) and the expanded catalogue (GWTC-2; Abbott et al. 2020), 50 gravitational wave merger events have been detected and the masses of merger components also suggest a mass gap between BHs and NSs (Fishbach, Essick & Holz 2020; LIGO Scientific Collaboration 2021).

Interacting binaries and gravitational wave sources are, however, very biased probes for constructing a census of compact objects. The conditions leading to mass transfer or mergers are rare, so such systems represent a very small fraction of the total BH binary population (Tanaka 2002; Wiktorowicz et al. 2019). Understanding interacting and merging binaries requires identifying and understanding the population of non-interacting binary BHs.

However, the detection of non-interacting BHs is inherently challenging due to their electromagnetically dark nature. There are estimates that 10^2–10^5 long-period BH binaries will be detectable with *Gaia* astrometry (Breivik, Chatterjee & Larson 2017; Mashian & Loeb 2017; Yalinewich et al. 2018; Yamaguchi et al. 2018). Short-period, detached BHs with non-compact object companions may be detected in photometric surveys through a combination of microlensing events, ellipsoidal variations, and relativistic beaming (Masuda & Hotokezaka 2019; Gomel, Faigler & Mazeh 2020). Microlensing surveys can also be used to identify compact object candidates that are not in binaries (see Paczynski 1986; Gould & Yee 2014; Abdurrahman, Stephens & Lu 2021).

Because dynamical processes in dense stellar systems can drive the formation of BH binaries, globular clusters should have more BH binaries than the field per unit stellar mass (Askar, Arca Sedda & Giersz 2018). Giesers et al. (2018) identified a BH with $M = 4.36 \pm 0.41\,M_\odot$ in the globular cluster NGC 3201 and two additional BHs in NGC 3201 were reported in Giesers et al. (2019).

Several candidate non-interacting BHs in the field have been reported and debated in the last few years. Liu et al. (2019) detected

★ E-mail: rowan.90@osu.edu

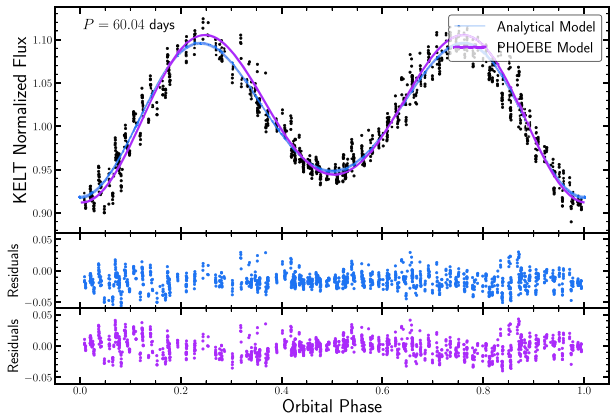

Figure 1. KELT light curve for V723 Mon (Jayasinghe et al. 2021a). The analytical model used in Section 2 (blue), is consistent with the PHOEBE model fit by Jayasinghe et al. (2021a) (purple). The middle panel shows the residuals of the analytical model and the bottom panel shows the residuals of the PHOEBE model.

radial velocity (RV) variations in a B star, LB-1, suggesting the presence of a 68^{+11}_{-13} $M_\odot$ BH companion. Subsequent analysis has suggested a lower companion mass 2–3 $M_\odot$ BH, but the nature of the system remains unclear (El-Badry & Quataert 2020; Irrgang et al. 2020; Shenar et al. 2020; Lennon et al. 2021). Rivinius et al. (2020) claimed that HR 6819 is a hierarchical triple containing stellar mass BH, but the system was later suggested to be a binary of a slowly rotating B and a rapidly rotating Be star (El-Badry & Quataert 2021).

Other systems are still best described with non-interacting BH companions. Thompson et al. (2019) reported a stellar mass BH with $M = 3.3^{+2.8}_{-0.7}$ $M_\odot$ orbiting the spotted red giant 2MASS J05215658+4359220. They identified this system by searching sparse Apache Point Observatory Galactic Evolution Experiment (APOGEE) RV measurements for systems with high binary mass function and photometric variability in All-Sky Automated Survey for Supernovae (ASAS-SN). Most recently, Jayasinghe et al. (2021a) combined archival spectroscopic orbits with photometric observations of ellipsoidal variability to identify a 3.04 ± 0.06 $M_\odot$ BH orbiting the nearby, bright red giant V723 Mon. In both cases, spectroscopic surveys were the first step of the compact object search.

Another approach to search for compact objects in binary systems is to search for ellipsoidal variables (ELLs) in time-domain photometric surveys. Ellipsoidal variability occurs due to the tidal distortions of a star by its binary companion. Many interacting binaries should also show ellipsoidal variations, but measuring them is complicated by the emission from the accretion. X-ray transients such as A0620-00 (Cantrell et al. 2008) and ASASSN-18ey (Tucker et al. 2018) can have multiple optical states resulting in brightness drifts and light curves that change between cycles. In quiescent phases, the ellipsoidal variations can sometimes be measured as in V4641 Sgr (Markwardt, Swank & Marshall 1999; Orosz et al. 2001).

ELL light curves have a characteristic double-peaked structure with typically uneven minima. Fig. 1 shows the KELT (Pepper et al. 2007) light curve of V723 Mon (Jayasinghe et al. 2021a) as an example. While RV measurements are needed to confirm the nature of the variability (Soszynski et al. 2004), a photometric search for ELLs offers a practical starting point to study the Milky Way stellar mass BH population. Here, we search for ELLs using the ASAS-SN (Shappee et al. 2014; Kochanek et al. 2017; Jayasinghe et al. 2018). In Section 2.1, we describe the initial selection of targets from the ASAS-SN variable stars catalogue. We use the analytical model of Morris & Naftilan (1993) to search for ELL candidates in Section 2. ELL light curves can closely resemble those of eclipsing binaries, spotted variables, and RV Tauri stars. In Section 2.3, we describe how we visually inspect the initial candidates to produce our final catalogue. In Section 2.4, we describe 15 systems that show both ellipsoidal variations and eclipses. We combine the photometric properties of the observed stars from the Anders et al. (2019) `StarHorse` catalogue with our ELL model amplitudes to derive minimum companion masses in Section 2.5. We cross-match our ELL catalogue with RV catalogues and X-ray catalogues in Section 3. Finally, we present a summary of our results in Section 4.

2 SEARCHING FOR ELLIPSOIDAL VARIABLES

The ASAS-SN *V*-band observations made between 2012 and mid 2018 have been used to classify $\sim 426\,000$ variable stars, including $\sim 219\,000$ new discoveries (Jayasinghe et al. 2021b). Since the number of ELL variables is expected to be small relative to other types of variability, ELLs were not included in the random forest classification used by Jayasinghe et al. (2019). Some ELLs were visually identified as a part of Pawlak et al. (2019), but most will have been classified as eclipsing binaries or rotational variables. We use an analytical model to search for ELL light curves in ASAS-SN and validate the candidates with visual inspection. In the absence of RV measurements, we combine the ELL model with photometric estimates of the stellar properties to derive a minimum companion mass for the ELL candidates.

2.1 ASAS-SN search catalogue

We begin with the ASAS-SN catalogue of variable stars (Jayasinghe et al. 2018). Since ELLs can be confused with other variable classifications, we make a broad selection from the catalogue in classification probability $P_{\rm class}$ and period P. We selected the following stars for our search:

(i) W UMa (EW) binaries with $P_{\rm class} > 0.4$
(ii) Beta Lyrae (EB) binaries with $P_{\rm class} > 0.4$
(iii) Rotational variables (ROT) with $P_{\rm class} > 0.4$
(iv) Semiregular variables (SR) with $P_{\rm class} > 0.4$ and $P < 60$ d
(v) Ellipsoidal variables (ELL) with $P_{\rm class} > 0.9$ and amplitude < 0.4

The $P < 60$ d cutoff for SRs is chosen to reduce contamination from dust-producing pulsating AGB and RGB stars (Alard et al. 2001; McDonald et al. 2018; Jayasinghe et al. 2021b). This led to an initial search catalogue of 194 879 stars. We use the periods from Jayasinghe et al. (2019) to phase-fold the *V*-band light curves.

2.2 Analytical model for ellipsoidal modulations

We fit each light curve with a series of analytical models to identify the best ELL candidates. Ellipsoidal modulations have a characteristic double-peaked structure with uneven maxima where the fractional luminosity changes can be represented by a discrete

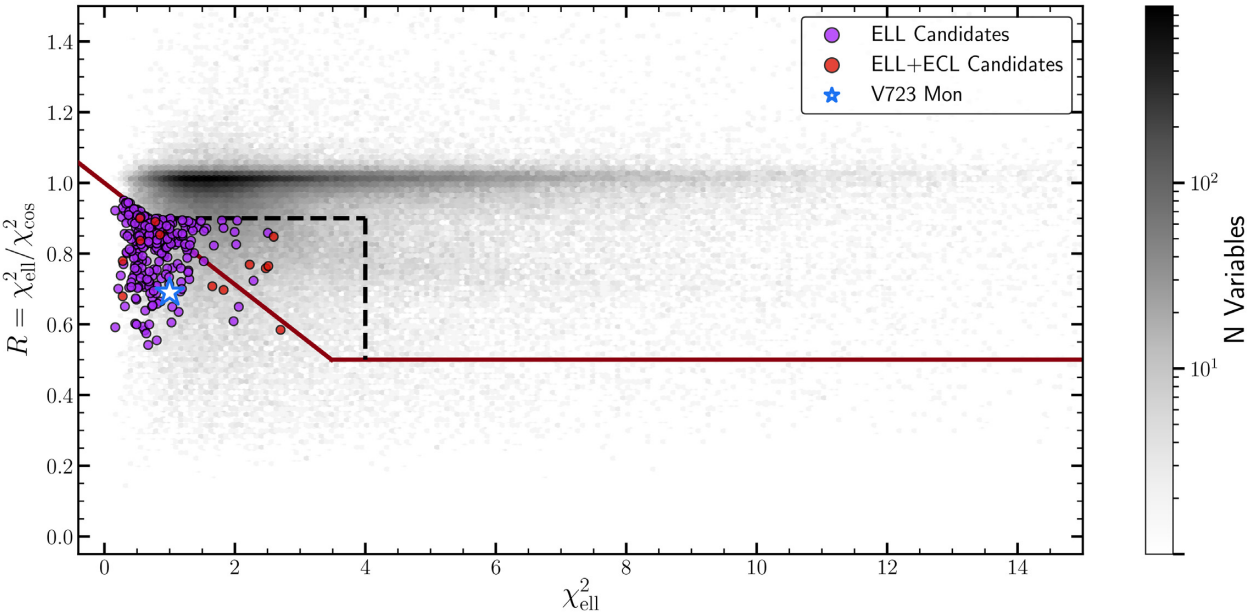

Figure 2. We compare the $\chi^2_{\rm ell}$ of the fit to the analytical model of ellipsoidal variability to the $\chi^2_{\rm cos}$ of a simple cosine fit. The red line indicates our visual inspection sample corresponding to ~ 5 per cent of the total sample. The V723 Mon KELT light curve (Jayasinghe et al. 2021a) is shown as a star and would be selected by this cut. Points below the red line are selected for visual inspection. Purple and red points are the ELL and ELL + ECL systems remaining after visual inspection. We also inspect stars in the region bounded by the black dotted lines to assess the effectiveness of the original cut. We find the majority of ELL candidates are selected by our original χ^2 criterion.

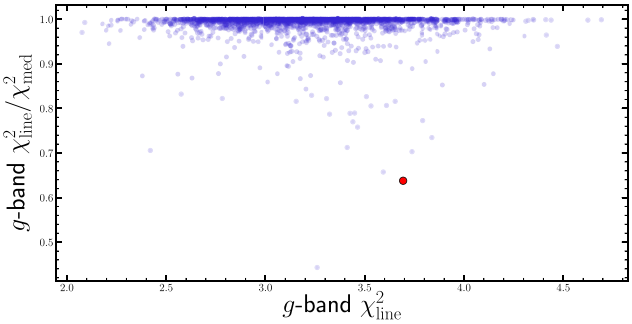

Figure 3. We use the χ^2 ratio of a linear fit $\chi^2_{\rm line}$ to a constant $\chi^2_{\rm med}$ to identify spotted stars with long-term variability. Blue points correspond to all stars selected from the ELL χ^2 ratio cut after visual inspection of the V-band data. The red point corresponds to ASASSN-V J021306.19−324658.8, a rotational variable identified during visual inspection and shown in Fig. 4.

Fourier series. The first three terms are

$$\begin{aligned}\frac{\Delta L}{\bar{L}} =& \frac{\alpha_1}{\bar{L}/L_0}\left(\frac{R_*}{a}\right)^4 q\left(4\sin i - 5\sin^3 i\right)\cos\phi \\ &- \frac{1}{\bar{L}/L_0}\left[\alpha_2\left(\frac{R_*}{a}\right)^3 q\sin^2 i\right. \\ &\left. + \beta_2\left(\frac{R_*}{a}\right)^5 q\left(6\sin^2 i - 7\sin^4 i\right)\right]\cos 2\phi \\ &- \frac{5}{3}\frac{\alpha_1}{\bar{L}/L_0}\left(\frac{R_*}{a}\right)^4 q\sin^3 i\cos 3\phi\end{aligned} \tag{1}$$

where R_* is the radius of the luminous primary, a is the binary semimajor axis, $q = M_2/M_1$ is the mass ratio of the secondary to the photometric primary, and i is the inclination (Morris & Naftilan 1993; Gomel et al. 2020). The orbital phase ϕ is defined such that

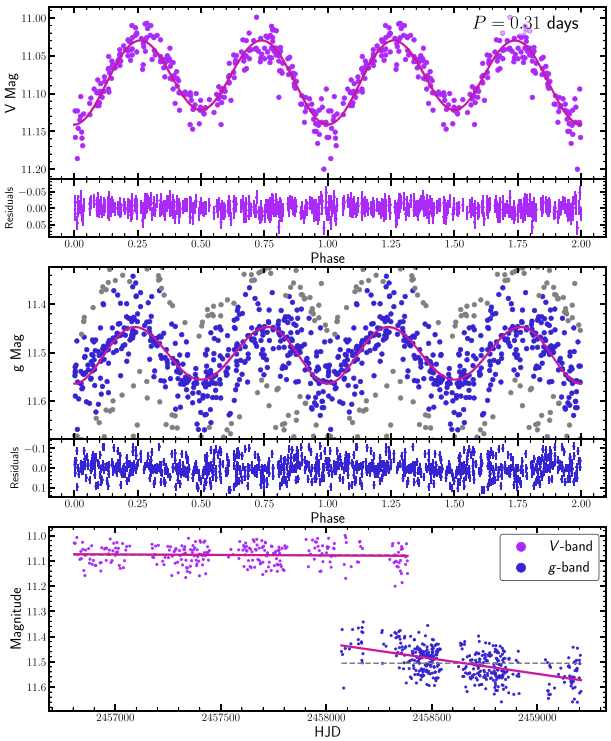

Figure 4. ASAS-SN V-band (top), g-band (middle), and unfolded (bottom) light curves for ASASSN-V J021306.19−324658.8. Solid lines in phase-folded light curves correspond to the ELL model. Grey points are points clipped at 5σ from the binned light curve. The bottom panels show the linear fits in time for each band (magenta line) compared to the median magnitude (grey line). The V-band light curve was selected as part of our visual inspection sample but is likely a spotted star because of the long-term evolution shown in average g-band flux.

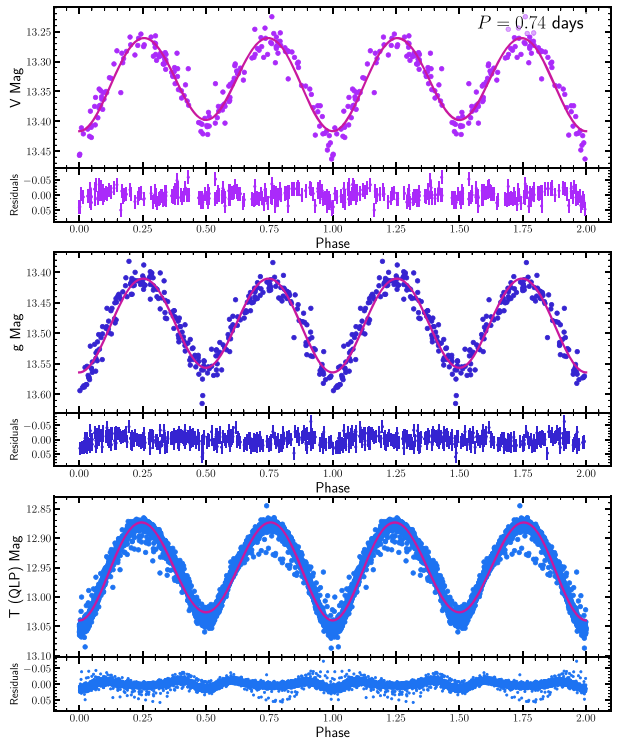

Figure 5. ASAS-SN *V*-band (top), *g*-band (middle), and *TESS* QLP (bottom) light curves for ASASSN-V J192943.61+641153.4. Solid lines in the light curves correspond to least-squares ELL fit. The smaller panels below each light curve show the residuals. This light curve is more consistent with an eclipsing binary than an ELL variable.

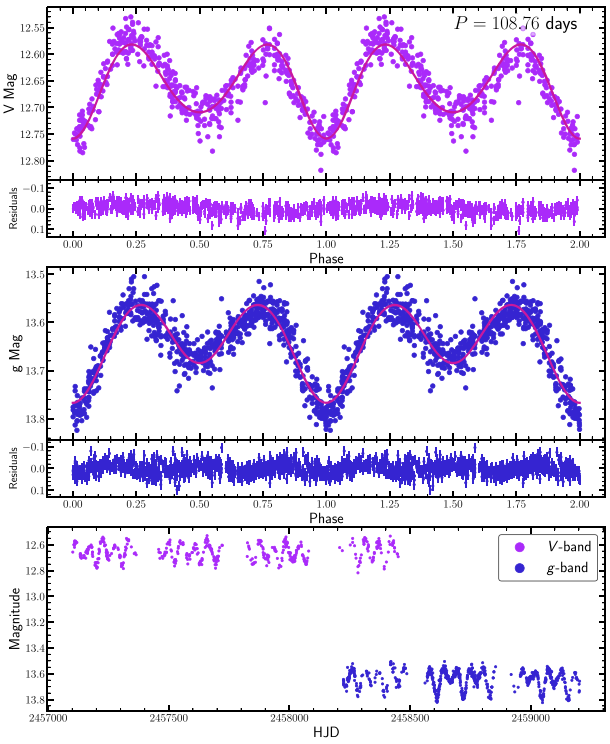

Figure 6. ASAS-SN *V*-band (top), *g*-band (middle), and unfolded (bottom) light curves for ASASSN-V J210204.31+394834.5. Solid lines in the light curves correspond to least-squares ELL fit. This light curve was selected as part of our visual inspection sample because of the uneven minima, but it is probably an RV Tauri variable.

the photometric minimum occurs at $\phi = 0$. The average luminosity $\bar{L}$ is given by

$$\bar{L} = L_0 \left(1 + \frac{1}{9}\alpha_2 \left(\frac{R_*}{a}\right)^3 (2+5q)\left(2 - 3\sin^2 i\right)\right) \quad (2)$$

and the coefficients

$$\alpha_1 = \frac{15u(2+\tau)}{32(3-u)},$$
$$\alpha_2 = \frac{3(15+u)(1+\tau)}{20(3-u)}, \text{ and} \quad (3)$$
$$\beta_2 = \frac{15(1-u)(3+\tau)}{64(3-u)}$$

depend on the linear-limb darkening coefficient u and the gravity darkening coefficient τ (Gomel et al. 2020). Both u and τ depend on the temperature, surface gravity, and composition of the star, where we use the tables from Claret & Bloemen (2011).

We use an approximate analytical model rather than detailed light-curve modelling tools (e.g. PHOEBE, Conroy et al. 2020) for speed. Fig. 1 compares a Markov chain Monte Carlo (MCMC) fit of the analytical model as compared to the PHOEBE light-curve model of the KELT light curve of V723 Mon in Jayasinghe et al. (2021a). The analytical model reproduces the PHOEBE model fit with sufficient accuracy for a fraction of the computational cost.

We first fit the analytical model in terms of the amplitudes of the three Fourier terms rather than the physical properties. Since the period calculated by Jayasinghe et al. (2019) may correspond to $P/2$ we fit the analytical model to light curves folded at both P and $2P$, and use the relative goodness of fit to determine which corresponds to the ELL period. We compare the $\chi^2_{\rm ell}$ of the ELL fit to a cosine fit with $\chi^2_{\rm cos}$ and compute the ratio $R = \chi^2_{\rm ell}/\chi^2_{\rm cos}$. ELLs with uneven minima will have a low $\chi^2_{\rm ell}$ and $R < 1$. Fig. 2 shows R as a function of $\chi^2_{\rm ell}$ for all variables in our search catalogue. Since we are interested in finding a relatively 'clean' sample of ELLs and not a complete catalogue of ELLs in ASAS-SN, we first make a cut, indicated by the red line, that encompasses ~ 5 per cent of the total sample. We visually inspect all light curves for variables that fall below this line.

We used two additional simple empirical cuts to help eliminate spotted variables. These stars often show drifts in their mean magnitude as the spots evolve. We computed a $\chi^2_{\rm med}$ of the light curve about the median magnitude and a $\chi^2_{\rm line}$ of a light curve about a linear fit in time. We expect spotted stars to have a ratio $R_{\rm LT} = \chi^2_{\rm line}/\chi^2_{\rm med} < 1$. Fig. 3 shows the distribution of stars in the g-band $\chi^2_{\rm line}$ and the ratio $\chi^2_{\rm line}/\chi^2_{\rm med}$. Stars with the ratio significantly below unity tend to be spotted stars, as illustrated by the example marked in Fig. 3 and shown in Fig. 4.

2.3 Light-curve visual inspection

While the χ^2 search method is effective at identifying ELLs with uneven minima, the majority of sources are still non-ELLs, with eclipsing binary, rotational variable, and long-period pulsator light curves significantly contaminating our sample. For the visual inspection, we supplement the *V*-band light curves with ASAS-SN *g*-band light curves and *TESS* light curves from either the SPOC (Caldwell et al. 2020) or QLP (Huang et al. 2020a,b) reduction pipelines. Before visual inspection, we phase all light curves such that the photometric minimum occurs at $\phi = 0$.

Table 1. 18 entries of the electronic table for ELL candidates. The ephemeris is defined for the photometric minimum at phase $\phi = 0$. The amplitude is measured between the 5th and 95th percentiles. We calculate e_2, M_0, and the minimum companion mass $M_{c,\min}$ in Section 2.5. The light curves are shown in Fig. 7.

ASAS-SN Name	Period (d)	Ephemeris	V Mag	Amplitude (mag)	M_* ($M_\odot$)	R_* ($R_\odot$)	e_2	M_0 ($M_\odot$)	$M_{c,\min}$ ($M_\odot$)
J152431.61−024128.4	118.04	2456591.8	11.87	0.12	1.02	51.82	0.026	5.03	0.21
J055840.45+355904.2	116.03	2456925.8	13.47	0.23	1.17	57.31	0.053	3.41	0.40
J230003.88+544229.6	115.72	2456956.6	14.51	0.22	1.09	47.31	0.047	2.21	0.53
J190444.42+392718.4	104.94	2456515.9	12.93	0.20	1.14	43.98	0.047	2.12	0.61
J142536.45−655257.5	67.08	2457429.9	13.83	0.19	1.28	61.50	0.037	18.03	0.09
J014838.40−571836.2	52.83	2456779.1	11.25	0.11	1.08	19.93	0.024	1.52	0.76
J100250.57−444358.8	44.99	2457388.1	13.56	0.25	1.03	21.57	0.056	1.14	0.93
J190107.88+360525.8	19.44	2456582.2	12.67	0.21	1.22	17.53	0.041	4.52	0.33
J015028.29+363449.2	17.39	2456634.9	11.37	0.18	1.09	14.16	0.042	2.94	0.40
J211215.61+461441.1	14.43	2457098.6	13.28	0.20	1.19	20.07	0.039	12.84	0.11
J042402.69+172034.8	13.94	2456224.9	12.20	0.07	1.07	12.59	0.020	6.79	0.17
J093807.91−464729.7	13.86	2457414.4	14.06	0.17	1.08	15.93	0.034	7.98	0.15
J081658.20+794246.8	9.30	2456678.9	13.59	0.20	1.06	8.39	0.044	2.00	0.56
J061849.14+170626.4	7.25	2457003.0	12.41	0.10	3.83	15.28	0.031	28.55	0.51
J194904.89+234219.9	2.52	2457077.7	12.53	0.13	5.60	26.50†	0.043	890.05	0.04
J051742.13+283602.1	0.94	2457007.6	12.49	0.11	2.09	4.43	0.033	38.40	0.11
J184156.58+222816.1	0.94	2457914.6	13.88	0.15	1.75	4.02	0.049	19.63	0.16
J173942.30−181421.3	0.85	2457070.6	14.13	0.22	1.60	3.56	0.071	11.46	0.22

†Radius derived from the `StarHorse` effective temperature, surface gravity, and metallicity is unphysical given the orbital period and estimated mass.

Spotted stars can have a double-peaked light curve with two uneven minima. Many also show long-term trends as illustrated by the variable in Fig. 4. The *g*-band light curves typically show more scatter and longer linear trends. This is likely due to the contribution of the calcium H and K lines created by chromospheric activity to the *g*-band.

Eclipsing binaries can also show two uneven minima separated by 0.5 in phase. Fig. 5 shows an example EW light curve, ASASSN-V J192943.61+641153.4, that was selected by our χ^2 search. In this case, the *TESS* light curve closely resembles known contact binaries such as YY Eri (fig. 3, Maceroni, Milano & Russo 1982). When *TESS* data are unavailable, the residuals in the *V*- and *g*-band light curves near the photometric minimum are effective at discriminating ELL from EB/EW. Comparing the three bands, the residuals of the ELL fit to ASASSN-V J192943.61+641153.4 show correlated residuals near $\phi = 0$.

At longer periods, RV Tauri stars are a potential source of false positives. RV Tauri variables are pulsating post-asymptotic branch or post-red giant branch stars that follow a known period–luminosity relation (Bódi & Kiss 2019). Compared to eclipsing binary light curves, RV Tauri variables are expected to show minima that are both asymmetric and uneven. Fig. 6 shows a likely RV Tauri variable (ASASSN-V J210204.31+394834.5). In this case, the asymmetric minima and uneven maxima both indicate that ASASSN-V J210204.31+394834.5 is unlikely to be an ELL.

After visually inspecting the stars selected by the red line in Fig. 2, we repeated the visual inspection process for a second region of the R–$\chi^2_{\rm ell}$ parameter space indicated by the dotted line to assess the effectiveness of this selection method. Since many more variables fall in this new parameter space, we restricted this sample to variables previously classified as ROT and SR. We find that the majority of our ELL candidates are found in our original selection region, confirming that the ratio of $\chi^2_{\rm ell}$ to $\chi^2_{\rm cos}$ is an effective metric to select ELL variables. After multiple rounds of visual inspection, we identified a total of 369 ELL candidates and an additional 15 ELLs with eclipses (ELL + ECL) discussed below.

The candidates are listed in Table 1 and Fig. 7 shows examples of their *V*-band light curves. Fig. 8 shows the period distribution for the ELL candidates. ELL candidates have periods ranging from 0.25 to 143.19 d with a median period of 9.3 d. While the sample before visual inspection has a single peak at $P \sim 0.6$ d, the final ELL candidate distribution shows three peaks. This distribution is consistent with the sample of OGLE ellipsoidal variables in the Galactic bulge (Soszyński et al. 2016; Gomel et al. 2021). The three peaks likely correspond to the conditions for observing ellipsoidal variability at different evolutionary stages. Fig. 9 shows the ELL and ELL + ECL candidates on a *Gaia* colour–magnitude diagram (CMD) with extinctions from `StarHorse` (Anders et al. 2019). Whereas tidal distortion of main-sequence stars can only produce observable ellipsoidal variability for systems with short-period orbits, red clump and giant branch stars can be distorted by companions in much larger orbits.

2.4 Ellipsoidal variables with eclipses

During visual inspection, we identified 15 variables that show both eclipses and ellipsoidal modulations (ELL + ECL). Although the observed eclipsing features show that the unseen companion is not a compact object, we include these systems for completeness and because they may be useful for other purposes. The phase of the binary is well constrained when fitting the analytical model in equation (1), so we expect any eclipses to occur at phase $\phi = 0$, when the companion eclipses the photometric primary, or at phase $\phi = 0.5$, when the photometric primary eclipses the companion. For the systems that we flagged as having eclipsing features at $\phi = 0$ and/or $\phi = 0.5$, we modified the ELL analytical model to include one or two boxcar components. The ELL + ECL model is fit using MCMC methods with the Python package `EMCEE` (Foreman-Mackey et al. 2013). The resulting eclipse width is used to estimate the eclipse duration given the orbital period. The eclipse duration and depth are included in Table 2 and Fig. 10 shows the 15 light curves with the modified ELL + ECL fit.

As compared to the ELL candidates, ELL + ECL systems typically have longer periods, with a median period of 11.86 d, and slightly higher $\chi^2_{\rm ell}$ (Fig. 2). The majority of ELL + ECL systems are also on the giant branch (Fig. 9). We are more successful at finding

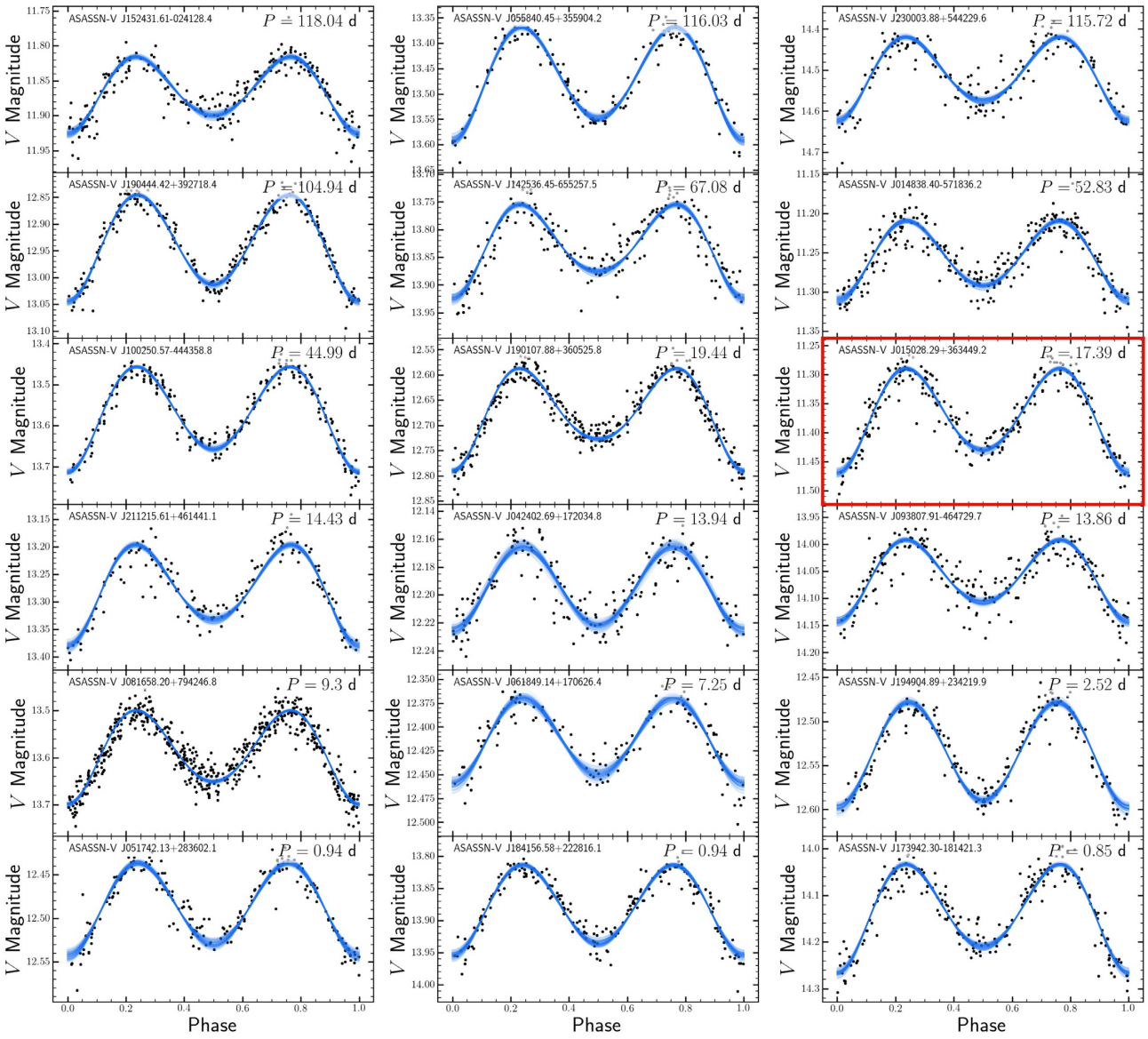

Figure 7. 18 randomly selected ELL candidate *V*-band light curves sorted by period. The period is given in upper right corner of each panel. 100 random samples of the MCMC posteriors computed are shown in blue. The MCMC corner plot for the panel highlighted in red (ASASSN-V J015028.29+363449.2) is shown in Fig. 11.

ELL + ECL systems at longer periods as compared to the ELL candidates.

2.5 Minimum companion mass

Without RV data we cannot fully confirm the ELL nature of the candidates or the properties of the companion stars. However, reliable parallaxes from *Gaia* Early Data Release 3 (EDR3; Gaia Collaboration 2016, 2021) and photometry have been used in both *Gaia* Data Release 2 (DR2; Gaia Collaboration 2018) and `StarHorse` (Queiroz et al. 2018; Anders et al. 2019) to estimate the stellar parameters.

The *Gaia* DR2 catalogue has luminosity, temperature, and radius measurements for 313 of the ELL candidates. These radii are computed using APSIS-Flame assuming an extinction of $A_G = 0$ (Andrae et al. 2018). Better estimates can be obtained from `StarHorse` (Queiroz et al. 2018) that uses a broader range of photometry to fit the stellar spectral energy distributions (SEDs) and then estimate masses, temperatures, surface gravities, and extinctions. Fig. 9 shows a CMD of the 356 ELL candidates in the Anders et al. (2019) catalogue. We used `Isoclassify` (Huber et al. 2017; Berger et al. 2020) to interpolate over the `MIST` (Paxton et al. 2011; Choi et al. 2016; Dotter 2016) model bolometric corrections to calculate the luminosity of each star given the estimated extinction, temperature, distance, and *G*-band magnitude. This allows us to calculate the stellar radius R_* given the Anders et al. (2019) $T_{\rm eff}$ measurements.

Next, we refit the *V*-band light curves of the candidates in terms of the underlying physical parameters in equation (1) using MCMC with `EMCEE` (Foreman-Mackey et al. 2013; Foreman-Mackey 2016). We use the *V*-band light curves rather than the *g*-band because of the longer baseline of observation. For each variable, we perform 50 000 iterations with 200 walkers. Initial positions are selected based on a least-squares fit. We sample over inclination, mass ratio, and (R_*/a). The photospheric parameters u and τ are held fixed from a linear

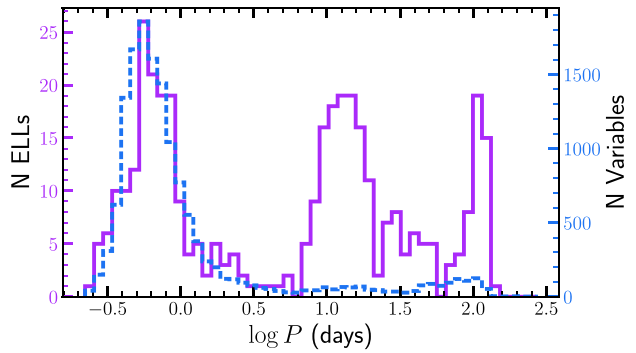

Figure 8. Period distribution for the ELL candidates (purple) and the initial candidates that were selected by the $\chi^2_{\rm ell}$ cut (blue). Periods range from 0.25 to 143.19 d. The median period is 9.3 d. While the period distribution of the initial candidates contains a single peak, we find a triple peaked distribution of ELL periods. These peaks correspond to different evolutionary stages as shown on the CMD in Fig. 9.

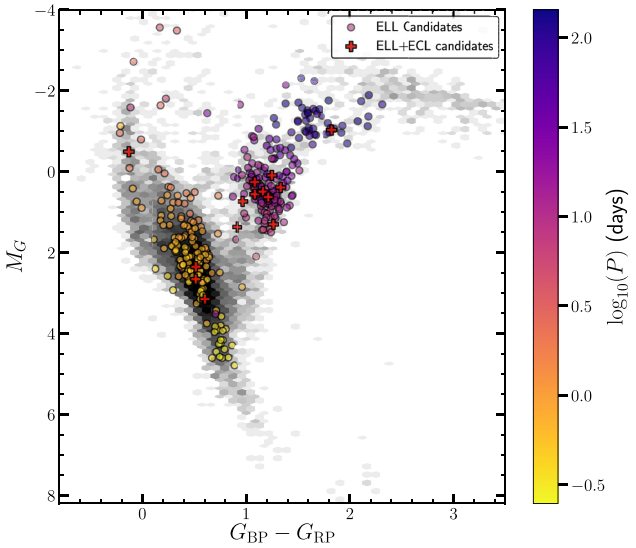

Figure 9. ELL and ELL + ECL variables on a *Gaia* CMD using the `StarHorse` extinction estimates. All of the variables that were visually inspected are shown in grey and the final ELL candidates are coloured by log P. The three peaks in the period distribution of Fig. 8 generally correspond to different evolutionary stages. ELL + ECL variables are shown in red and are not coloured by period.

interpolation over the Claret & Bloemen (2011) tables given the effective temperature, surface gravity, and metallicity estimates. We use a value of 2.0 km s^{-1} for the microturbulent velocity.

Fig. 11 shows the results for candidate ASASSN-V J015028.29+363449.2, whose light curve is shown in Fig. 7. The best-measured quantity related to the masses is the amplitude of the cos 2θ Fourier term

$$e_2 = q(R_*/a)^3. \tag{4}$$

The separate values of q and R_*/a, while constrained by the amplitudes of the other Fourier terms, are relatively degenerate. The `EMCEE` sampler is affine-invariant and appears to have little difficulty sampling the q-R_*/a parameter space despite the near degeneracy. We experimented with sampling in e_2 and either q or R_*/a but it appeared to make no practical difference.

Given the period P of the binary and the photometric estimate of the radius of the primary R_*, the total binary mass is

$$M_T = M_c + M_* = \frac{4\pi^2 R_*^3 q}{G P^2 e_2} \tag{5}$$

where M_c is the companion mass and M_* is the primary mass. Since the estimates of q are fairly degenerate with estimates of R_*/a, the quantity

$$M_0 = \frac{M_T}{q} = \frac{4\pi^2 R_*^3}{G P^2 e_2} \tag{6}$$

is the mass scale most reliably measured by the light-curve models. In terms of M_* and M_0, the companion mass is

$$M_c = \frac{M_*^2}{M_0 - M_*}. \tag{7}$$

The difference in the denominator tends to be very uncertain, so we focus on a more robust lower limit on the companion mass

$$M_c > M_{c,\rm min} = \frac{M_*^2}{M_0}, \tag{8}$$

Fig. 12 shows the distributions of the median posteriors for e_2, M_0, and $M_{c,\rm min}$. We find the median minimum companion mass is 0.2 M$_\odot$ and 14 systems have minimum companion masses greater than 1 M$_\odot$. In the absence of RV measurements, the minimum companion mass can be used to prioritize follow-up observations to search for non-interacting compact object binaries. ASAS-SN J095846.87−443947.1 has $M_{c,\ \rm min} = 136$ M$_\odot$, the largest in the candidate catalogue. While this outlying minimum mass estimate probably indicates that the main-sequence star is not an ELL, we do not reject any variables based on the mass estimates calculated from the photometric fits.

For systems where the companion is not a compact-object, the luminosity modulations given in equation (1) would also contain a constant flux, or 'third-light', term. With a single photometric band we cannot constrain the presence of modest amounts of additional constant flux from a companion. If present, it will reduce our estimate of the amplitude of the ellipsoidal variability, leading to an overestimate of the minimum mass in equation (8). The presence of such contamination can in many cases be constrained photometrically by whether the amplitude of the ellipsoidal variability changes with wavelength (Morris & Naftilan 1993).

We can also use known non-interacting compact object binary systems to place an additional check on our sorting method. We fit the V723 Mon KELT R-band light curve shown in Fig. 1 with the ELL analytical model. Using the fit $e_2 = 0.0493$, the `StarHorse` $M_* = 1.09$ M$_\odot$, and $R = 22.70$ R$_\odot$, we find the minimum companion mass is $M_c > 1.39$ M$_\odot$. Not only is this consistent with the mass measured by Jayasinghe et al. (2021a), but it is also higher than almost all ELL candidates in our catalogue, suggesting that such systems are rare.

We find 14 ELL candidates where the `StarHorse` radius estimates are unphysical given the orbital period of the binary. ASAS-SN J193909.43+232051.4, for example, has an orbital period of $P = 4.37$ d and a radius estimate of $R = 53.71$ R$_\odot$. This is the most luminous star on the upper-main sequence shown in Fig. 9 at $M_G = -3.55$ mag. All of these stars are within 10 degrees of the Galactic plane, suggesting increased extinction may result in less reliable `StarHorse` measurements. Stars with such unphysical radii are marked in Table 1. Many of the outlying stars in the M_0 and $M_{c,\ \rm min}$ distributions have inaccurate radii. ASAS-SN J193909.43+232051.4, for example, has $M_0 > 1000$ M$_\odot$ and $M_{c,\ \rm min} = 0.006$ M$_\odot$.

Table 2. Ellipsoidal variables with eclipses (ELL + ECL) sorted by period. We estimate the eclipse depth and duration by adding one or two boxcar functions to the ELL analytical model. For sources where there are two eclipsing features, we designate the primary eclipse to correspond to the deeper ELL model minimum.

ASAS-SN Name	Period (d)	Ephemeris	V Mag	Amplitude (mag)	Eclipse depth (mag)	Eclipse duration (d)	Secondary depth (mag)	Secondary duration (d)
J095548.46−514201.4	94.94	2457349.4	13.76	0.15	$0.021^{+0.033}_{-0.009}$	$5.498^{+8.375}_{-3.684}$		
J184906.69−392039.8	36.84	2456775.8	15.15	0.50	$0.095^{+0.111}_{-0.079}$	$3.128^{+3.416}_{-2.850}$	$0.056^{+0.071}_{-0.041}$	$2.581^{+3.126}_{-2.195}$
J101405.66−454458.6	34.15	2457422.3	14.41	0.31	$0.081^{+0.092}_{-0.070}$	$1.678^{+1.699}_{-1.656}$		
J081954.35−012713.9	33.79	2456594.7	13.98	0.40	$0.066^{+0.073}_{-0.058}$	$2.903^{+3.158}_{-2.682}$	$0.105^{+0.115}_{-0.096}$	$1.157^{+1.200}_{-1.114}$
J120959.21−462542.9	31.13	2456765.0	15.35	0.62	$0.094^{+0.106}_{-0.082}$	$2.352^{+2.382}_{-2.338}$	$0.101^{+0.114}_{-0.087}$	$2.120^{+2.166}_{-2.096}$
J060405.52−794630.1	15.67	2456778.3	11.69	0.29	$0.047^{+0.051}_{-0.043}$	$1.450^{+1.460}_{-1.440}$	$0.043^{+0.047}_{-0.039}$	$1.181^{+1.194}_{-1.170}$
J075030.20−053035.8	14.54	2456597.4	13.02	0.14	$0.018^{+0.034}_{-0.006}$	$0.316^{+0.762}_{-0.097}$		
J000321.41+383106.7	11.86	2456596.8	12.75	0.19	$0.038^{+0.042}_{-0.033}$	$0.862^{+0.938}_{-0.818}$	$0.033^{+0.038}_{-0.028}$	$0.576^{+0.645}_{-0.531}$
J183357.85+423725.2	8.72	2456592.2	12.37	0.16	$0.049^{+0.055}_{-0.043}$	$0.445^{+0.494}_{-0.395}$		
J131011.62−235415.1	8.20	2456788.4	12.08	0.31	$0.091^{+0.096}_{-0.086}$	$0.649^{+0.669}_{-0.629}$		
J120622.28+304056.6	6.86	2456780.5	11.70	0.08	$0.036^{+0.043}_{-0.030}$	$0.344^{+0.421}_{-0.289}$		
J055644.29+094108.1	2.30	2457036.9	13.30	0.13	$0.044^{+0.054}_{-0.034}$	$0.186^{+0.210}_{-0.151}$	$0.041^{+0.062}_{-0.022}$	$0.052^{+0.133}_{-0.020}$
J073600.57+373306.7	1.03	2456615.9	11.74	0.07	$0.043^{+0.050}_{-0.035}$	$0.050^{+0.060}_{-0.043}$		
J182814.03+613840.5	0.76	2456674.5	14.07	0.13	$0.020^{+0.027}_{-0.013}$	$0.062^{+0.073}_{-0.043}$		
J211632.71−122442.9	0.44	2456236.6	13.35	0.20	$0.022^{+0.030}_{-0.014}$	$0.028^{+0.031}_{-0.024}$		

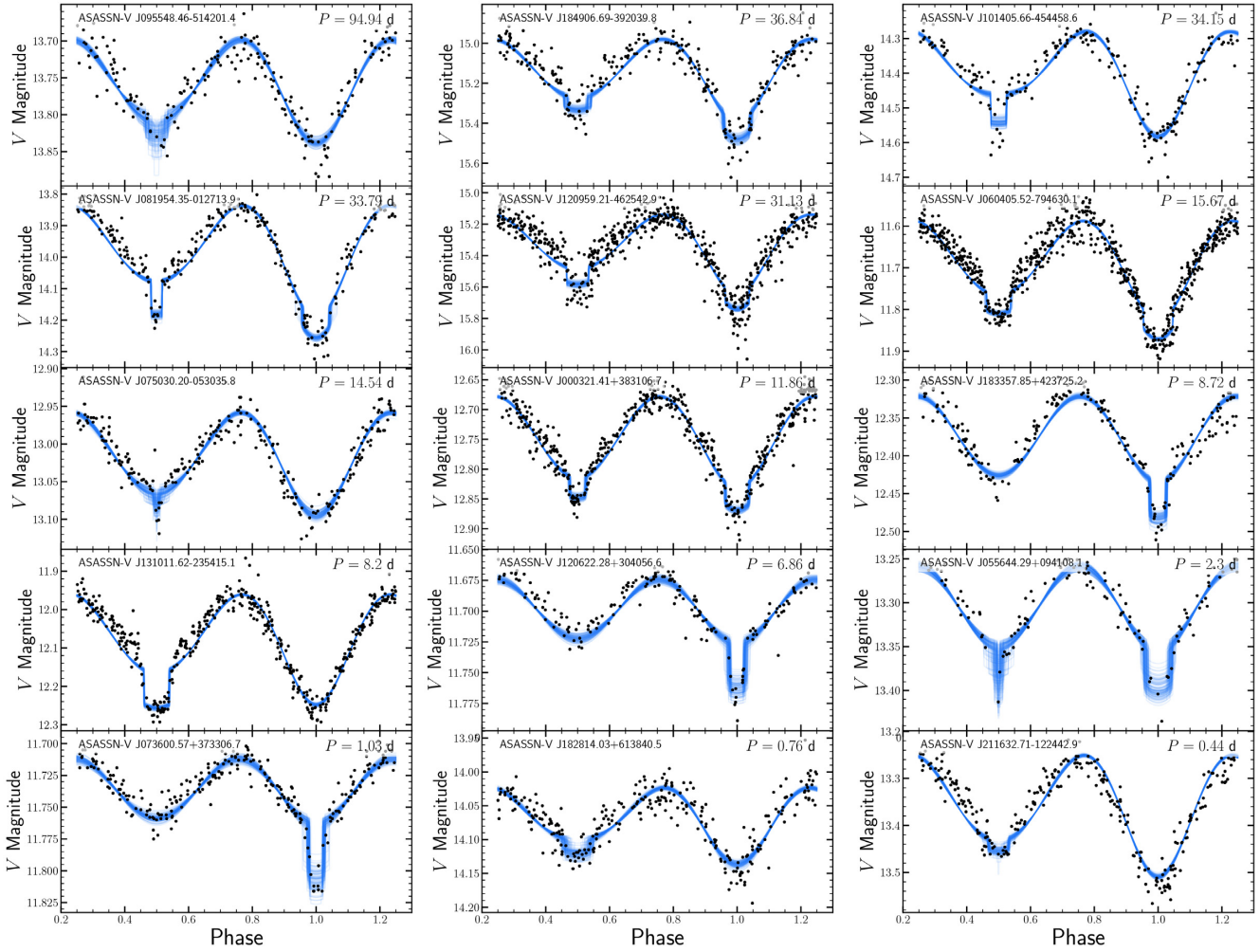

Figure 10. Light curves of 15 candidates that show eclipses in addition to the ellipsoidal modulations. 100 random samples of the MCMC posteriors are shown in blue. We use the same definition of phase, where $\phi = 0$ corresponds to the ELL minimum, but adjust the range of the axis to better illustrate the eclipses. Eclipse depth and duration are given in Table 2.

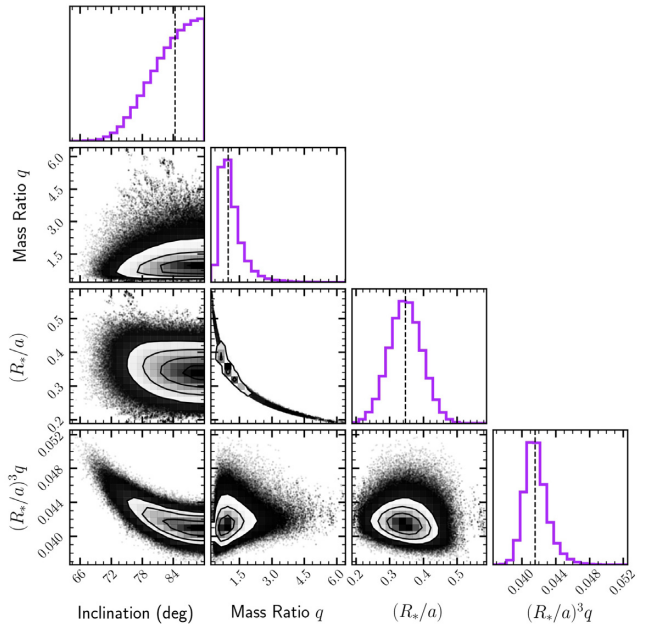

Figure 11. MCMC posteriors for ASASSN-V J015028.29+363449.2. The vertical lines on the histograms show the median value. We use the posterior on $e_2 = (R_*/a)^3 q$ to sort ELL candidates. The light curve of this system is shown in the highlighted panel of Fig. 7.

3 RADIAL VELOCITIES AND X-RAYS

We next search for systems with existing multi-epoch RV measurements. We cross-match our ELL candidate catalogue with the Large Sky Area Multi-Object Fibre Spectroscopic Telescope Survey Data Release 5 (LAMOST DR5; Luo et al. 2015; Yuan et al. 2015), the APOGEE Data Release 16 (DR16; Holtzman et al. 2015; García Pérez et al. 2016; Ahumada et al. 2020), and the the Sixth Data Release of the Radial Velocity Experiment (RAVE DR6; Steinmetz et al. 2020a,b) with a matching radius of 5″.0. We find 13 APOGEE DR16 cross-matches, nine of which have multiple observations. We find 57 LAMOST DR5 cross-matches, 12 of which have multiple observations. We find 13 RAVE DR6 cross-matches, none of which have multiple observations.

For the systems with multiple RV measurements that have a phase separation $\Delta\phi > 0.25$, we fit a circular orbit to the RV data using the photometric period and phase. Since $\phi = 0$ corresponds to photometric minimum, the maximum of the RV curve will occur at $\phi = 0.75$. We use the resulting semi-amplitude K to calculate the mass function

$$f(M) = \frac{PK^3}{2\pi G} = \frac{M_c^3 \sin^3 i}{(M_* + M_c)^2}. \quad (9)$$

If we again assume the `StarHorse` mass estimates for M_* we can calculate the mass of the companion M_c. The inclination and $\sin^3 i$ posteriors from the MCMC fit to the ELL analytical model are broad for many candidates, such as the example shown in Fig. 11, so we simply use an edge-on inclination to calculate the minimum companion mass for the RV fits. Table 3 lists the ELL candidates with multiple RV observations and the derived amplitudes K, mass functions f, and M_c. Fig. 13 shows the light curves and phased RV observations for two of these systems, ASASSN-V J150333.84+210420.4 and J001532.90+384119.9. None of these systems yield companion masses that are promising candidates for NS or BH companions, although they could be non-interacting white dwarf companions.

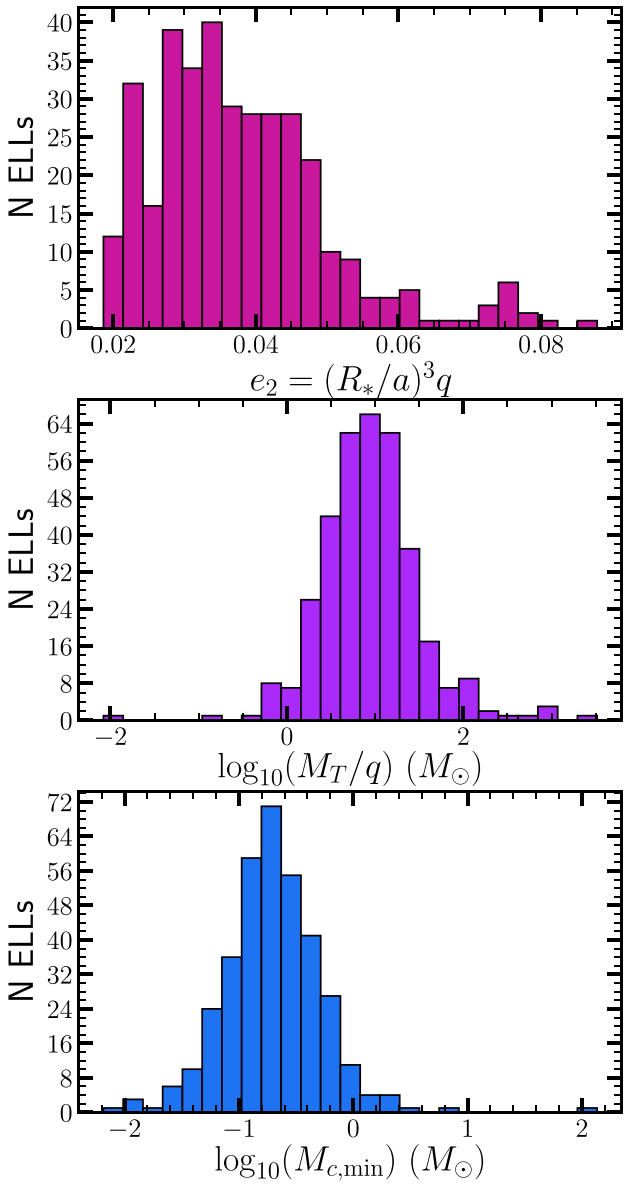

Figure 12. Distributions of e_2, M_T/q and $M_{c,\min}$ for ELL candidates with `StarHorse` estimates of the stellar properties.

ASASSN-V J150333.84+210420.4 has the most RV points (29 APOGEE DR16 and one LAMOST DR5) and $f(M) = 0.048\,M_\odot$. Given the `StarHorse` mass $M_L = 1.07\,M_\odot$ this implies a companion mass $M_c \sim 0.49\,M_\odot$. While this companion is unlikely to be a BH, this system does offer a sanity check on our minimum mass estimation of $M_{c,\min} = 0.39\,M_\odot$. ASASSN-V J001532.90+384119.9 was identified by Gu et al. (2019) and Zheng et al. (2019) as a candidate non-interacting compact object and has four LAMOST observations separated by 0.34 in phase. The mass function is $f(M) = 0.32\,M_\odot$ suggesting a companion mass $M_c = 1.17$ for the `StarHorse` luminous star mass $M_* = 1.07\,M_\odot$. This is again consistent with the minimum mass $M_{c,\min} = 0.81\,M_\odot$ calculated from the ELL analytical model.

Table 3. ELL Candidates with Multiple RV observations from APOGEE DR16 and LAMOST DR5 sorted by period. Four have Max($\Delta\phi$) > 0.25 but are poorly fit by a circular model so we do not include K, f, or $M_{c,\mathrm{RV}}$. The V723 Mon RV results from Jayasinghe et al. (2021a) are included for comparison.

ASAS-SN Name	Period (d)	N_{RV}	Max($\Delta\phi$)	K (km s^{-1})	$f(M)$ ($M_\odot$)	$M_{c,\mathrm{RV}}$ ($M_\odot$)	$M_{c,\mathrm{min}}$ ($M_\odot$)	Survey
J055450.78+242657.3	143.19	3	0.41	8.75	0.01	0.26	0.07	APOGEE
J041857.27+400108.6	119.43	2	0.03					APOGEE
J152431.61−024128.4	118.04	3	0.31	12.53	0.02	0.36	0.21	RAVE, LAMOST
J114807.73−020920.5	113.42	2	0.46	22.64	0.14	0.70	0.17	LAMOST
J190444.42+392718.4	104.94	2	0.44	31.29	0.33	1.23	0.61	APOGEE, LAMOST
J221959.83+673236.6	76.69	2	0.04					APOGEE
J093300.84+341709.2	44.68	5	0.16					APOGEE, LAMOST
J140925.52+512653.7	29.97	3	0.06					LAMOST
J001532.90+384119.9	27.56	4	0.34	48.28	0.32	1.17	0.81	LAMOST
J032653.26+005506.7	19.32	5	0.26	33.17	0.07	0.60	0.15	APOGEE
J042402.69+172034.8	13.94	4	0.36	64.44	0.39	1.29	0.17	APOGEE, LAMOST
J150333.84+210420.4	13.35	30	0.50	32.53	0.05	0.49	0.39	APOGEE, LAMOST
J081658.20+794246.8	9.30	3	0.38	47.86	0.11	0.69	0.56	APOGEE
J065624.05+245825.6	4.81	3	0.23					APOGEE
J062252.43+034920.5	0.77	4	0.00					LAMOST
J075654.91+474622.9	0.66	3	0.40	90.05	0.05	0.58	0.57	LAMOST
J101909.73+414611.1	0.45	3	0.45	8.96	<0.01	0.04	0.14	LAMOST
J150355.74−011623.2	0.43	2	0.00					LAMOST
J081929.94+090258.3	0.37	2	0.21					LAMOST
J080826.59−055109.9	1.19	2	0.38					LAMOST
J084328.53+402247.5	1.02	4	0.40					LAMOST
J061635.56+231909.4	0.87	3	0.31					LAMOST
J161803.43+420416.8	0.32	4	0.48					APOGEE
V723 Mon	60.04	128	0.5	65.15	1.72	3.04	1.39	(Jayasinghe et al. 2021a)

There are four ELL candidates that have Max($\Delta\phi$) > 0.25 that are not well-fit by the circular orbit model: ASASSN-V J080826.59 − 055109.9, J084328.53 + 402247.5, J061635.56 + 231909.4, and J161803.43 + 420416.8. Two of these, ASASSN-V J080826.59 − 055109.9 and J084328.53 + 402247.5, have LAMOST observations with maximum Δ(RV) comparable to the RV uncertainty. J061635.56 + 231909.4 has three LAMOST points, two of which have $\Delta\phi$ < 0.05 but Δ(RV) > 128 km s^{-1}. The four APOGEE RV measurements for J161803.43 + 420416.8 have a maximum Δ(RV) = 6.2 km s^{-1} and are also not well-fit by circular orbit model. While a poor RV fit may indicate that the system is not an ELL, we do not remove any ELL candidates on the basis of the sparse APOGEE/LAMOST RV measurements. These systems are listed in Table 3 but we do not report the RV fits.

Finally, we cross-match our ELL candidate catalogue with the Master X-Ray Catalogue provided by HEASARC[1] and with the Swift X-ray Telescope Point Source Catalogue (2XPs; Evans et al. 2020). We found that nine of the ELL candidates are likely X-ray sources, although the larger offset *ROSAT* matches should probably be confirmed. Table 4 lists the sources and their estimated X-ray luminosities given the *Gaia* EDR3 parallaxes.

X-ray emission could correspond to accretion in a compact object binary. In their quiescent states, X-ray binaries have been detected with relatively low luminosities $<10^{32}$ erg s^{-1}. Rodriguez et al. (2020) reported the X-ray observations of GS 2000+25 in the quiescent state with luminosity $L = 1.1^{+1.0}_{-0.7} \times 10^{30}(d/2\ \mathrm{kpc})^2$ erg s^{-1}. Alternatively, high-energy emission may be evidence of chromospheric activity or coronal emission in eclipsing binaries (e.g. Bedford et al. 1990). The presence of X-ray emission does not offer clear distinctions between ELL and non-ELL variables, but may serve as a useful metric for prioritizing RV follow-up of ELL candidates.

[1] https://heasarc.gsfc.nasa.gov/W3Browse/all/xray.html

4 CONCLUSIONS

Previous searches for non-interacting compact object binaries have started from RV surveys to identify variables with a large mass function (Liu et al. 2019; Thompson et al. 2019; Yi, Sun & Gu 2019; Jayasinghe et al. 2021a). Here, we take advantage of multiyear all-sky photometry from ASAS-SN to search almost 200 000 variables for ellipsoidal variability. The final result is a catalogue of 369 ELL candidates and 15 ELL + ECL candidates.

Our search method identifies light curves with uneven minima by comparing an analytical model of ellipsoidal modulations to a cosine fit. We perform multiple rounds of visual inspection to remove eclipsing binaries and rotational variables from the catalogue. By combining the analytical model with masses and radii from the Anders et al. (2019) `StarHorse` catalogue, we derive conservative estimate of the minimum companion masses for the ELL candidates.

RV observations are a necessary next step to evaluate the nature of the unseen companion. The subset of ELL candidates with multiple RV measurements offers a sanity check on the minimum mass as a metric to sort ELL candidates. Where we can make the comparison, the minimum companion mass calculated from the ELL analytical model is consistent with the mass estimated from the RV semi-amplitude, suggesting the minimum companion mass is a viable metric to sort ELL candidates for follow-up. Jayasinghe et al. (2021a) report that V723 Mon has $M = 3.3^{+2.8}_{-0.7}$ $M_\odot$ and our minimum mass estimate is $M_{c,\mathrm{min}} = 1.39$ $M_\odot$. The majority of our ELL candidates have a lower minimum companion mass, suggesting that systems like V723 Mon are rare. Systems with higher companion mass limits are likely the best targets for RV follow-up in the search for non-interacting compact objects.

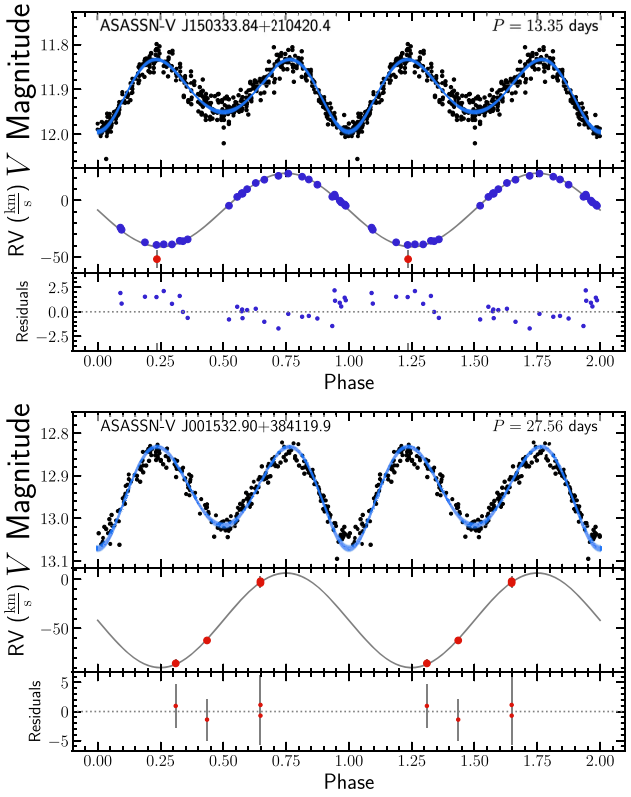

Figure 13. ASAS-SN *V*-band light curves and RV measurements for ASASSN-V J150333.84+210420.4 (top) and J001532.90+384119.9 (bottom). APOGEE DR16 measurements are shown in blue and LAMOST DR5 are in red. The blue lines show the least-squares fit to the ELL analytical model. The grey lines show the best-fitting circular orbit given the photometric period and phase where $\phi = 0$ is defined as the photometric minimum.

ACKNOWLEDGEMENTS

We thank the Las Cumbres Observatory and its staff for its continuing support of the ASAS-SN project. The ASAS-SN operations are supported by the Gordon and Betty Moore Foundation through grant GBMF5490 to the Ohio State University.

DMR is supported by The Ohio State University Graduate Fellowship. KZS, TJ, and CSK are supported by NSF grants AST-1814440 and AST-1908570. TJ acknowledges support from the Ohio State Presidential Fellowship. TAT is supported in part by NASA grant 80NSSC20K0531. Support for JLP is provided in part by the Ministry of Economy, Development, and Tourism's Millennium Science Initiative through grant IC120009, awarded to The Millennium Institute of Astrophysics, MAS.

This work has made use of data from the European Space Agency (ESA) mission *Gaia* (https://www.cosmos.esa.int/gaia), processed by the *Gaia* Data Processing and Analysis Consortium (DPAC, https://www.cosmos.esa.int/web/gaia/dpac/consortium). Funding for the DPAC has been provided by national institutions, in particular the institutions participating in the *Gaia* Multilateral Agreement. This research has made use of the SIMBAD data base, operated at CDS, Strasbourg, France. Guoshoujing Telescope (the Large Sky Area Multi-Object Fiber Spectroscopic Telescope LAMOST) is a National Major Scientific Project built by the Chinese Academy of Sciences. Funding for the project has been provided by the National Development and Reform Commission. LAMOST is operated and managed by the National Astronomical Observatories, Chinese Academy of Sciences.

Funding for the Sloan Digital Sky Survey IV has been provided by the Alfred P. Sloan Foundation, the U.S. Department of Energy Office of Science, and the Participating Institutions.

SDSS-IV acknowledges support and resources from the Center for High Performance Computing at the University of Utah. The SDSS website is www.sdss.org.

SDSS-IV is managed by the Astrophysical Research Consortium for the Participating Institutions of the SDSS Collaboration including the Brazilian Participation Group, the Carnegie Institution for Science, Carnegie Mellon University, Center for Astrophysics|Harvard & Smithsonian, the Chilean Participation Group, the French Participation Group, Instituto de Astrofísica de Canarias, The Johns Hopkins University, Kavli Institute for the Physics and Mathematics of the Universe (IPMU)/University of Tokyo, the Korean Participation Group, Lawrence Berkeley National Laboratory, Leibniz Institut für Astrophysik Potsdam (AIP), Max-Planck-Institut für Astronomie (MPIA Heidelberg), Max-Planck-Institut für Astrophysik (MPA Garching), Max-Planck-Institut für Extraterrestrische Physik (MPE), National Astronomical Observatories of China, New Mexico State University, New York University, University of Notre Dame, Observatário Nacional/MCTI, The Ohio State University, Pennsylvania State University, Shanghai Astronomical Observatory, United Kingdom Participation Group, Universidad Nacional Autónoma de México, University of Arizona, University of Colorado Boulder, University of Oxford, University of Portsmouth, University of Utah, University of Virginia, University of Washington, University of Wisconsin, Vanderbilt University, and Yale University. This research made use of Astropy, a community-developed core Python package for Astronomy.

DATA AVAILABILITY

The ASAS-SN photometric data underlying this article are available on the ASAS-SN Photometry Database (https://asas-sn.os u.edu/ph

Table 4. ELL Candidates with X-Ray cross-matches from the Master X-ray Catalogue and Swift 2XPS.

ASAS-SN Name	Telescope	Period (d)	X-ray Luminosity (erg s^{-1})	Separation (arcsec)
ASASSN-V J172630.51−381304.4	XMM–NEWTON	18.31	3.37×10^{30}	1.19
ASASSN-V J015028.29+363449.2	ROSAT	17.39	1.80×10^{31}	13.27
ASASSN-V J010522.46+482502.4	Swift	16.85	2.11×10^{32}	1.77
ASASSN-V J161454.69−513604.8	XMM–NEWTON	15.76	3.76×10^{30}	3.65
ASASSN-V J155416.74+081826.6	Swift	10.09	2.09×10^{31}	1.95
ASASSN-V J032202.62−511248.8	CHANDRA	8.74	5.24×10^{30}	0.34
ASASSN-V J183142.73+444829.1	ROSAT	0.41	1.34×10^{31}	9.30
ASASSN-V J023618.76+615619.7	XMM–NEWTON	0.31	3.10×10^{30}	1.29
ASASSN-V J060831.46−442417.5	ROSAT	0.28	5.54×10^{30}	4.71

otometry) and the ASAS-SN variable stars data base (https://asas-sn.osu.edu/variables). The spectroscopic data sets underlying this article were accessed from sources in the public domain: APOGEE (https://www.sdss.org/dr16/), LAMOST (http://dr5.lamost.org/), and RAVE (https://www.rave-survey.org/). The data underlying this article are available in the article and in its online supplementary material.

REFERENCES

Abbott B. P. et al., 2016, Phys. Rev. Lett., 116, 061102
Abbott B. P. et al., 2017, Phys. Rev. Lett., 119, 161101
Abbott B. P. et al., 2019, Phys. Rev. X, 9, 031040
Abbott R. P. et al., 2021, Phys. Rev. X 11 021053
Abdurrahman F. N., Stephens H. F., Lu J. R., 2021, ApJ, 912, 146
Adams S. M., Kochanek C. S., Gerke J. R., Stanek K. Z., Dai X., 2017, MNRAS, 468, 4968
Ahumada R. et al., 2020, ApJS, 249, 3
Alard C. et al., 2001, ApJ, 552, 289
Anders F. et al., 2019, A&A, 628, A94
Andrae R. et al., 2018, A&A, 616, A8
Askar A., Arca Sedda M., Giersz M., 2018, MNRAS, 478, 1844
Bailyn C. D., Jain R. K., Coppi P., Orosz J. A., 1998, ApJ, 499, 367
Basinger C. M., Kochanek C. S., Adams S. M., Dai X., Stanek K. Z., 2020, preprint (arXiv:2007.15658)
Bedford D. K., Jeffries R. D., Geyer E. H., Vilhu O., 1990, MNRAS, 243, 557
Berger T. A., Huber D., van Saders J. L., Gaidos E., Tayar J., Kraus A. L., 2020, AJ, 159, 280
Bódi A., Kiss L. L., 2019, ApJ, 872, 60
Breivik K., Chatterjee S., Larson S. L., 2017, ApJ, 850, L13
Caldwell D. A. et al., 2020, Res. Notes Am. Astron. Soc., 4, 201
Cantrell A. G., Bailyn C. D., McClintock J. E., Orosz J. A., 2008, ApJ, 673, L159
Choi J., Dotter A., Conroy C., Cantiello M., Paxton B., Johnson B. D., 2016, ApJ, 823, 102
Claret A., Bloemen S., 2011, A&A, 529, A75
Conroy K. E. et al., 2020, ApJS, 250, 34
Corral-Santana J. M., Casares J., Muñoz-Darias T., Bauer F. E., Martínez-Pais I. G., Russell D. M., 2016, A&A, 587, A61
Dotter A., 2016, ApJS, 222, 8
El-Badry K., Quataert E., 2020, MNRAS, 493, L22
El-Badry K., Quataert E., 2021, MNRAS, 502, 3436
Evans P. A. et al., 2020, ApJS, 247, 54
Farr W. M., Sravan N., Cantrell A., Kreidberg L., Bailyn C. D., Mandel I., Kalogera V., 2011, ApJ, 741, 103
Fishbach M., Essick R., Holz D. E., 2020, ApJ, 899, L8
Foreman-Mackey D., 2016, J. Open Source Softw., 1, 24
Foreman-Mackey D., Hogg D. W., Lang D., Goodman J., 2013, PASP, 125, 306
Gaia Collaboration, 2016, A&A, 595, A1
Gaia Collaboration, 2018, A&A, 616, A1
Gaia Collaboration, 2021, A&A, 649, A1
García Pérez A. E. et al., 2016, AJ, 151, 144
Gerke J. R., Kochanek C. S., Stanek K. Z., 2015, MNRAS, 450, 3289
Giesers B. et al., 2018, MNRAS, 475, L15
Giesers B. et al., 2019, A&A, 632, A3
Gomel R., Faigler S., Mazeh T., 2021, MNRAS, 501, 2822
Gomel R., Faigler S., Mazeh T., Pawlak M., 2021, MNRAS, 504, 5907
Gould A., Yee J. C., 2014, ApJ, 784, 64
Gu W.-M. et al., 2019, ApJ, 872, L20
Holtzman J. A. et al., 2015, AJ, 150, 148
Huang C. X. et al., 2020a, Res. Notes Am. Astron. Soc., 4, 204
Huang C. X. et al., 2020b, Res. Notes Am. Astron. Soc., 4, 206
Huber D. et al., 2017, ApJ, 844, 102
Irrgang A., Geier S., Kreuzer S., Pelisoli I., Heber U., 2020, A&A, 633, L5
Jayasinghe T. et al., 2018, MNRAS, 477, 3145
Jayasinghe T. et al., 2019, MNRAS, 486, 1907
Jayasinghe T. et al., 2021a, MNRAS, 504, 2577
Jayasinghe T. et al., 2021b, MNRAS, 503, 200
Kochanek C. S., 2014, ApJ, 785, 28
Kochanek C. S., Beacom J. F., Kistler M. D., Prieto J. L., Stanek K. Z., Thompson T. A., Yüksel H., 2008, ApJ, 684, 1336
Kochanek C. S. et al., 2017, PASP, 129, 104502
Lennon D. J. et al., 2021, A&A, 649, A167
LIGO Scientific Collaboration, 2021, ApJ, 913, L7
Liu J. et al., 2019, Nature, 575, 618
Luo A. L. et al., 2015, Res. Astron. Astrophys., 15, 1095
Maceroni C., Milano L., Russo G., 1982, A&AS, 49, 123
McDonald I., De Beck E., Zijlstra A. A., Lagadec E., 2018, MNRAS, 481, 4984
Markwardt C. B., Swank J. H., Marshall F. E., 1999, IAU Circ., 7120, 1
Mashian N., Loeb A., 2017, MNRAS, 470, 2611
Masuda K., Hotokezaka K., 2019, ApJ, 883, 169
Morris S. L., Naftilan S. A., 1993, ApJ, 419, 344
Neustadt J. M. M., Kochanek C. S., Stanek K. Z., Basinger C. M., Jayasinghe T., Garling C. T., Adams S. M., Gerke J., 2021, preprint (arXiv:2104.03318)
Orosz J. A. et al., 2001, ApJ, 555, 489
Özel F., Psaltis D., Narayan R., McClintock J. E., 2010, ApJ, 725, 1918
Paczynski B., 1986, ApJ, 304, 1
Pawlak M. et al., 2019, MNRAS, 487, 5932
Paxton B., Bildsten L., Dotter A., Herwig F., Lesaffre P., Timmes F., 2011, ApJS, 192, 3
Pejcha O., Thompson T. A., 2015, ApJ, 801, 90
Pepper J. et al., 2007, PASP, 119, 923
Pooley D., Kumar P., Wheeler J. C., Grossan B., 2018, ApJ, 859, L23
Queiroz A. B. A. et al., 2018, MNRAS, 476, 2556
Remillard R. A., McClintock J. E., 2006, ARA&A, 44, 49
Rivinius T., Baade D., Hadrava P., Heida M., Klement R., 2020, A&A, 637, L3
Rodriguez J. et al., 2020, ApJ, 889, 58
Shappee B. J. et al., 2014, ApJ, 788, 48
Shenar T. et al., 2020, A&A, 639, L6
Soszynski I. et al., 2004, Acta Astron., 54, 347
Soszyński I. et al., 2016, Acta Astron., 66, 405
Steinmetz M. et al., 2020a, AJ, 160, 82
Steinmetz M. et al., 2020b, AJ, 160, 83
Tanaka Y., 2002, Black-Hole Binaries. Springer, Dordrecht, p. 839
Thompson T. A. et al., 2019, Science, 366, 637
Timmes F. X., Woosley S. E., Weaver T. A., 1996, ApJ, 457, 834
Tucker M. A. et al., 2018, ApJ, 867, L9
Ugliano M., Janka H.-T., Marek A., Arcones A., 2012, ApJ, 757, 69
Wiktorowicz G., Wyrzykowski Ł., Chruslinska M., Klencki J., Rybicki K. A., Belczynski K., 2019, ApJ, 885, 1
Yalinewich A., Beniamini P., Hotokezaka K., Zhu W., 2018, MNRAS, 481, 930
Yamaguchi M. S., Kawanaka N., Bulik T., Piran T., 2018, ApJ, 861, 21
Yi T., Sun M., Gu W.-M., 2019, ApJ, 886, 97
Yuan H. B. et al., 2015, MNRAS, 448, 855
Zheng L.-L. et al., 2019, AJ, 158, 179

SUPPORTING INFORMATION

Supplementary data are available at *MNRAS* online.

Table 1. 18 entries of the electronic table for ELL candidates.

Please note: Oxford University Press is not responsible for the content or functionality of any supporting materials supplied by the authors. Any queries (other than missing material) should be directed to the corresponding author for the article.

This paper has been typeset from a TEX/LATEX file prepared by the author.